

Zone Refining of Ultrahigh-Purity Sodium Iodide for Low-Background Detectors

Burkhant Suerfu^{1,*}, Frank Calaprice,² and Michael Souza^{2,3}

¹*Department of Physics, University of California, Berkeley, Berkeley, California 94720, USA*

²*Department of Physics, Princeton University, Princeton, New Jersey 08544, USA*

³*Department of Chemistry, Princeton University, Princeton, New Jersey 08544, USA*

(Received 14 May 2021; revised 14 June 2021; accepted 1 July 2021; published 26 July 2021)

There has been a growing interest in ultrahigh-purity low-background NaI(Tl) crystals for dark-matter direct searches. Past research indicates that zone refining is an efficient and scalable way to purify NaI. In particular, K and Rb—two elements with radioisotopes that can cause scintillation backgrounds—can be efficiently removed by zone refining. However, zone refining has never been demonstrated for ultrahigh-purity NaI, which has become commercially available recently. In this paper, we show that many common metallic impurities can be efficiently removed via zone refining. A numerical model for predicting the final impurity distribution is developed and used to fit the inductively coupled plasma mass spectrometry (ICPMS) measurement data to determine the segregation coefficient and the initial concentration. Under this scheme, the segregation coefficient for K is estimated to be 0.57, indicating that zone refining is still effective in removing K from ultrahigh-purity NaI. As zone refining tends to move the impurities to one end, elements with concentrations too low to be measured directly in the unprocessed powder can potentially be detected in the end due to the enrichment. We also present an analysis technique to estimate the initial concentrations of impurities with partial data, which effectively enhances the sensitivity of the spectrometer. Using this technique, the initial concentration of ^{85}Rb is estimated to be between 5 parts per trillion (ppt) and 14 ppt at the 90% confidence level (CL), at least 14 times lower than the detection limit of ICPMS and 7 times lower than the current most stringent limit set by the DAMA collaboration by direct counting of radioactive ^{87}Rb . These results imply that zone refining is a key technique in developing next-generation NaI-based crystal scintillators for dark-matter direct detection.

DOI: [10.1103/PhysRevApplied.16.014060](https://doi.org/10.1103/PhysRevApplied.16.014060)

I. INTRODUCTION

Thallium-activated sodium iodide NaI(Tl) crystal is one of the most important and widely used scintillators in the fields of radiation detection and gamma spectroscopy. In recent years, there has been a growing interest in ultrahigh-purity NaI(Tl) crystals for dark-matter searches [1–5]. In these experiments, trace amounts of radioactive impurities—in particular, ^{40}K , ^{210}Pb and ^{3}H —can lead to background events in the energy region of interest. Ultrahigh-purity NaI powder with sub-parts-per-million metallic impurities is commercially available but the purity level is not yet sufficient for efficient dark-matter searches and further purification is desired.

Since the pioneering work of Pfann in 1952 [6], zone refining has been used to purify silicon and germanium for the semiconductor industry. In the zone-refining process, a narrow region of an ingot is melted and the molten

zone is traversed across the ingot. As the zone moves and the ingot solidifies, impurities—also called solutes—will redistribute such that the ratio of impurity concentration in the solid over that in the liquid remains constant. This constant is known as the segregation coefficient. The overall effect of the moving zone is that impurities are moved to one end of the ingot.

Later, the technology of zone refining was extended to other elements and compounds, including alkali halide salts. In 1960, Gross showed that many alkali and alkali earth impurities can be separated and removed from alkali iodides by zone refining [7]. However, due to the limitations of the assay technology, his work was done with dopants at 100 ppm. The effectiveness of zone refining at the parts per billion (ppb) level remains to be demonstrated. In this study, we investigate the effectiveness of zone refining in purifying commercial ultrahigh-purity NaI powder and we develop relevant quantitative simulation and data analysis techniques to estimate the segregation coefficients (k) and the average initial impurity concentrations (C_0) of common impurities in the NaI powder.

*suerfu@alumni.princeton.edu

II. EXPERIMENTAL PROCEDURE

For this study, 744 g of low-potassium ultrahigh-purity NaI powder from Sigma-Aldrich is carefully and thoroughly dried and sealed in a carefully cleaned synthetic fused-silica crucible and zone refined for 53 passes over approximately two weeks.

A. Crucible preparation and powder drying

To avoid contamination by impurities diffusing out of the crucible [8,9], a 1.5-in.-diameter 4-ft-long synthetic fused-silica crucible is used to seal and contain the ingot during the zone refining [9]. The crucible is cleaned by rinsing with 5% by volume hydrofluoric acid, followed by 5% by volume high-purity hydrochloric acid and deionized water. Subsequently, the crucible is vacuum baked at 400 °C to remove surface-adsorbed water.

To remove residual water from the ultrahigh-purity powder, the powder is first loaded into a 3-in.-diameter 2-ft-long fused-silica tube in a glove box purged with boil-off nitrogen and vacuum baked for one week at several stages of increasing temperatures, starting at room temperature. A detailed operational procedure is outlined in Ref. [9].

B. Powder drying and treatment with silicon tetrachloride

Trace amounts of Na₂O and NaOH can cause the ingot to stick to the crucible and make the extraction difficult. To remove Na₂O and NaOH already present in the powder prior to drying, the dried NaI powder is further melted under a silicon tetrachloride (SiCl₄) atmosphere in the cleaned and dried crucible to be used for zone refining [9,10]. The setup used is illustrated in Fig. 1.

The NaI powder is first loaded into the crucible inside the glove box and two fused-silica plugs—one with a

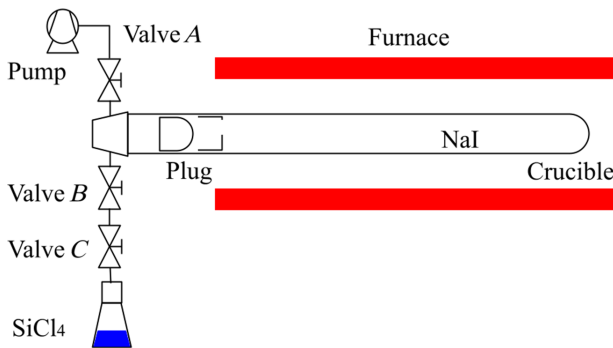


FIG. 1. The NaI powder is melted under a SiCl₄ atmosphere prior to zone refining. The plug on the right is used to introduce SiCl₄ vapor through the vent hole on the topside while preventing the back flow of the molten NaI. The plug on the left is used to hermetically seal the crucible once the powder has been treated with SiCl₄.

vent hole—are placed inside the crucible. A Pyrex vacuum adapter with two valves is attached to the open end of the crucible by compression fitting before it is taken out of the glove box. The assembly is placed horizontally and pumped to high vacuum using a turbomolecular pump via one of the two valves on the Pyrex adapter (valve A). Once the vacuum level reaches 10⁻⁵ mbar, the plug with the vent hole is fused to the crucible with a torch. A 50-ml flask containing SiCl₄ is attached to the other valve on the adapter (valve B) and the section containing the NaI powder is inserted into a horizontal furnace. The temperature of the furnace is slowly increased to 800 °C. When the temperature reaches 450 °C, valve A is closed and the valves between the SiCl₄ and the NaI powder (valves B and C) are opened to introduce the SiCl₄ vapor. After 1 h at 800 °C, the oven temperature is ramped down to 400 °C and the crucible is sealed using the other fused-silica plug so that some SiCl₄ vapor remains in the crucible during zone refining.

C. Zone refining

The sealed crucible is taken to the Mellen Company in Concord, New Hampshire for zone refining. In total, 53 zone passes are carried out at a rate of 2 in.h⁻¹ (Fig. 2). During the zone refining, the crucible remains sealed to prevent the introduction of additional contaminants. After zone refining, the crucible is brought back to Princeton. Samples are cut from different locations of the ingot and sent to Seastar Chemicals for assay with inductively coupled plasma mass spectroscopy (ICPMS). Prior to measurement, the samples are first rinsed with high-purity ethanol and deionized water to remove surface contaminants introduced during the sample cutting, packing, and shipment. The distribution of the impurity concentration is then compared to the expected distribution from the numerical model to estimate the segregation coefficient k and the average initial concentration C_0 .

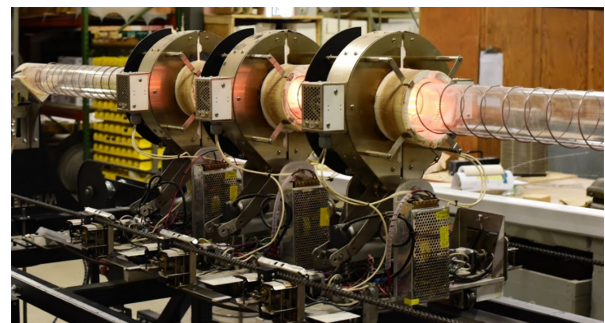


FIG. 2. Zone refining in progress at the Mellen Company with three zones. The crucible is placed inside a fused-silica preheater tube maintained at 300 °C by a resistive wire wound around the preheater tube.

III. NUMERICAL MODEL

Since there is no established analytical solution of the solute distribution for an arbitrary cross-section profile and an arbitrary number of zone passes, we develop a numerical model to simulate the final solute distribution [9]. In this numerical model, the entire ingot is divided into multiple cells with equal width, as illustrated in Fig. 3. To make the simulation easier, the overall length of the ingot is normalized to the total number of cells N and the width of the molten zone w is expressed as the integer number of cells spanned by the zone (see Fig. 3).

Let h_j , A_j , and C_j denote the width, the cross-section area, and the solute concentration of the j th cell, respectively. Two variables, M and V , are used to keep track of the total mass of solute and the total volume of the molten zone, respectively. Assuming that cells $i+1$ to $i+w$ are molten as in Fig. 3, the following relations exist:

$$C_i \leftarrow k \frac{M}{V}, \quad (1)$$

$$M \leftarrow M - A_i h_i C_i + A_{i+w} h_{i+w} C_{i+w}, \quad (2)$$

$$V \leftarrow V - A_i h_i + A_{i+w} h_{i+w}, \quad (3)$$

where \leftarrow is the assignment operator and k is the (effective) segregation coefficient, defined as the ratio of solute concentrations in the solid and the liquid phase. Equation (1) sets the solute concentration in the solidified i th cell based on the definition of k , whereas Eqs. (2) and (3) update M and V with the loss of solute due to the solidified i th cell and the gain of solute due to the newly melted $(i+w)$ th cell. To simulate one cycle of zone purification, the above relations are applied incrementally to each cell, starting from the beginning. Special care is taken at both ends: at the beginning of the ingot, M and V are initialized to the

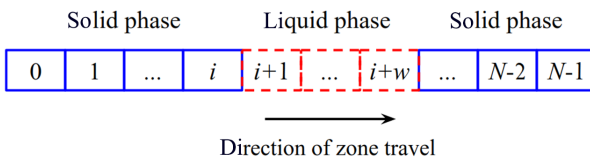


FIG. 3. The ingot is divided into N cells with equal width. Solid blue cells represent solidified sections of the ingot and the dashed red cells represent the molten-liquid zone. Two arrays, A_j and C_j , are used to denote the cross-section area and the solute concentration of the j th cell. When the left boundary of the zone travels from i to $i+1$, cell i solidifies and its solute concentration is given by k times the solute concentration of the molten-liquid zone [Eq. (1)]. As the right boundary advances to $(i+w)$ th cell, the solute concentration and total volume of the molten zone are updated based on the volume and the amount of solutes in the newly melted cell [Eqs. (2) and (3)]. To simulate the entire zone-refining process, the molten zone is swept across the entire ingot incrementally and the appropriate boundary relation is applied at each step.

sum of the respective quantities in the first w cells, since M and V will keep rising until the first zone solidifies:

$$M \leftarrow \sum_{i=0}^{w-1} A_i h_i C_i, \quad (4)$$

$$V \leftarrow \sum_{i=0}^{w-1} A_i h_i. \quad (5)$$

At the other end, the terms representing the gain due to the newly melted cell in Eqs. (2) and (3) are left out, since no new material is melted as the zone moves:

$$M \leftarrow M - A_i h_i C_i, \quad (6)$$

$$V \leftarrow V - A_i h_i. \quad (7)$$

The above operation can be applied repeatedly to simulate multiple zone passes. As an illustration, Fig. 4 shows the solute distributions in an ingot with uniform cross-section area after different numbers of zone passes. With this numerical approach, it is also straightforward to account for nonuniform initial solute distribution and a nonuniform ingot cross-section area (e.g., the tip of a crystal grown by the vertical Bridgman method, where the crucible is tapered). This algorithm is a reasonable description of the zone-refining process when (1) the segregation coefficient is constant over the solute concentrations of interest, (2) the solute redistribution is dominated by zone refining instead of vapor transport or diffusion, and (3) the change of cross-section profile in the process is negligible.

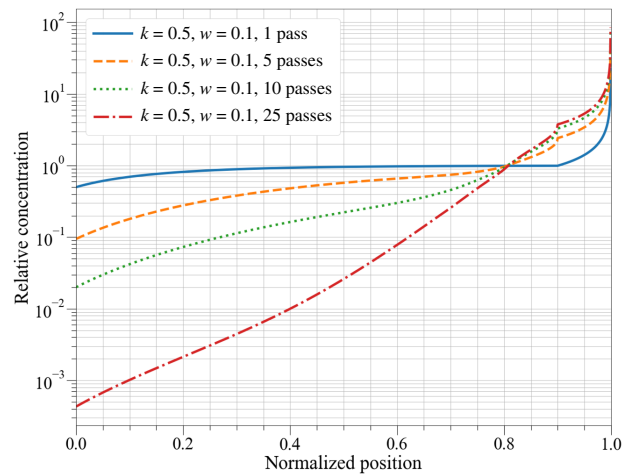


FIG. 4. The numerically calculated solute distributions after 1, 5, 10, and 25 zone passes. The segregation coefficient is assumed to be 0.5 and the zone width 10% of the ingot length. The initial average solute concentration is normalized to 1. As zone refining progresses, more and more impurities are pushed to the end of the ingot.

IV. DATA ANALYSIS

Since the unprocessed powder has impurity concentrations that are already near the detection threshold, the concentrations of many elements in the first half of the ingot are expected to be below the ICPMS detection limit. In addition, the concentrations of most solutes are expected to vary more rapidly toward the end of the ingot. Therefore, instead of taking samples from equally spaced positions, one sample is taken from the beginning of the ingot and other four samples are taken from roughly equally spaced positions in the latter half of the ingot. In the numerical model, the zone width is assumed to be 2 in. based on visual measurement. The number of zone passes is taken to be 53, consistent with the experiment. The cross-section profile of the ingot after zone refining is measured carefully and used in the numerical model.

To estimate k and C_0 of various elements in NaI, the numerical model is used to fit the measured position-dependent impurity concentration of each element by minimizing χ^2 . This procedure is repeated for different zone widths to account for up to 25% uncertainty in the zone width. Good to excellent agreement is obtained between the data and the best-fit model for many elements, with a few exceptions. Figure 5 shows, as an example, the ICPMS data and the best-fit model distribution of ^{39}K .

To avoid local minima and to obtain an accurate estimate of the uncertainties, the parameters corresponding to the minimum χ^2 are determined by a grid search in k - C_0 space. Once the global minima are located, the boundary of the $\Delta\chi^2 = 2.3$ contour is used as the associated upper

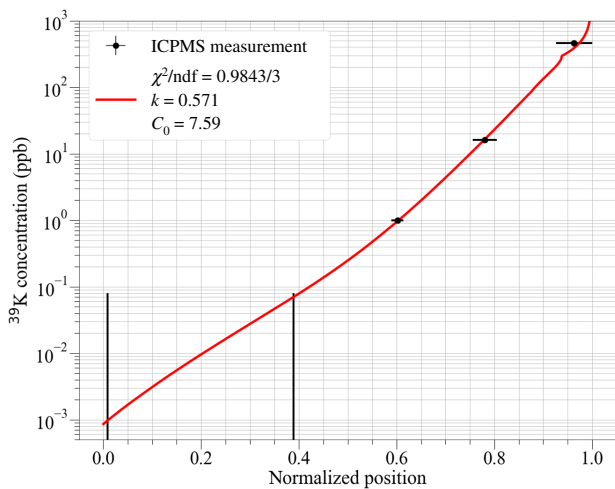


FIG. 5. The distribution of the concentration of ^{39}K as a function of the position. The position is measured from the beginning of the ingot where zone refining starts. The geometrical center of each sample is taken as the x coordinate of the data point and the size of the sample as the x error. The solid curve represents the best fit to the data.

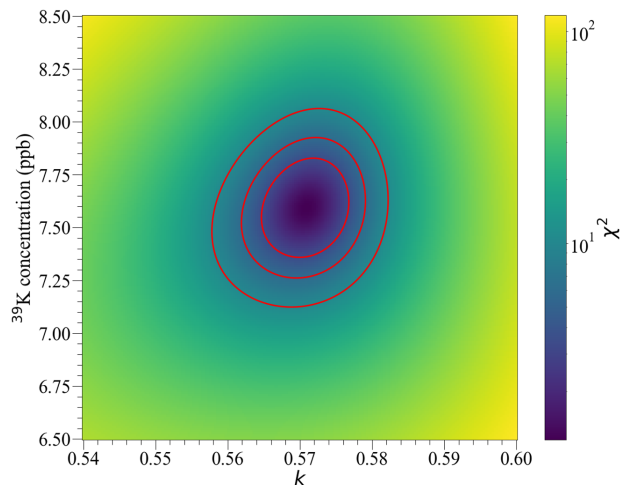


FIG. 6. The ^{39}K χ^2 map obtained by grid search in k - C_0 space. The χ^2 map is characterized by a well-defined global minimum, since the ^{39}K concentration is above the spectrometer detection limit at three different locations, allowing for simultaneous determination of k and C_0 . The three contour lines correspond to 1- σ , 90% CL, and 99% CL.

and lower 1- σ errors. The χ^2 map of ^{39}K obtained as the result of the grid search is illustrated in Fig. 6 along with 1- σ , 90% CL, and 99% CL contours.

When computing the χ^2 , the effect of the finite geometrical size of each sample is taken into account by fitting the average of the model distribution over the physical dimension of the sample instead of pointwise comparison. When there is more than one sample with an impurity concentration above the detection threshold, both pointwise evaluation and averaging over the physical extent of the sample yield similar results. However, when only one sample yields a concentration above the detection threshold, pointwise comparison will lead to the divergence of C_0 . This is illustrated in Fig. 7 using ^{85}Rb data.

A. Treatment of partial data

When two or more than two samples yield impurity concentrations above the detection limit, both parameters can be determined with relative ease. Figure 6 shows the χ^2 map for the ^{39}K distribution in Fig. 5, which belongs to this case. The χ^2 map is characterized by a well-defined global minimum.

When only one sample at the end of the ingot yields an impurity concentration above the detection limit, it is not possible to determine either of the parameters from the fit. This is because the available information can only be used to derive an upper limit for k —two values of k cannot be distinguished as long as they are both small enough to move a certain amount of impurity such that the concentrations at other sample locations are below the detection

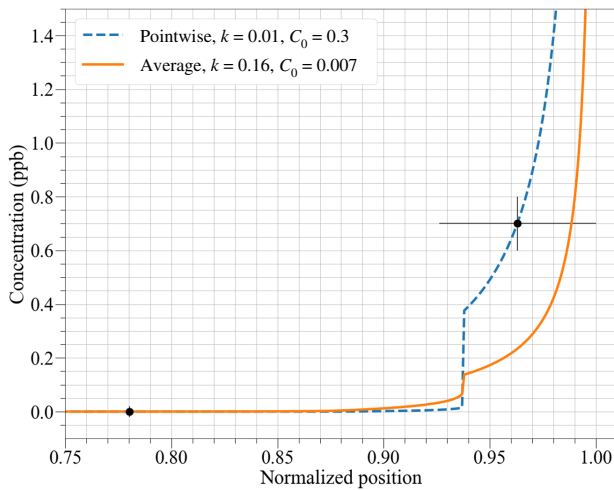


FIG. 7. The pointwise comparison of ^{85}Rb data leads to overestimation of C_0 . ^{85}Rb is detected only in the last sample at the end of the ingot after 53 zone passes. Since the concentration varies rapidly near the end, the true concentration-weighted center differs significantly from the geometrical middle of the sample. When the middle of the last sample is used as the x coordinate in a pointwise χ^2 computation, the distribution that matches exactly at the last data point is favored. Since the first four data points are all upper limits, k can take an arbitrarily small value at the cost of increased C_0 , thereby leading to overestimation of C_0 (dashed blue line). To treat this case properly, χ^2 should be computed using the average of the model distribution (solid orange line).

limit. Note that this scenario does not necessarily imply that zone refining is more efficient, especially when the concentration in the last sample is close to the detection limit.

However, even in this scenario, an upper limit for k and a confidence interval for C_0 can be found. This is because C_0 is constrained from below—the total amount of impurity cannot be less than that detected in the last sample alone. If the upper limits are small compared to the last data point, zone refining is very efficient and the majority of the impurities should be concentrated on the end. Thus, the amount of impurity remaining in other parts of the ingot are several orders of magnitude smaller and the associated errors are small as well. In other words, the uncertainty in C_0 due to the uncertainty in k is small. This is illustrated by the flat band of C_0 as k goes to 0 in Fig. 8. In this case, a relatively narrow confidence interval for C_0 can be derived.

The above analysis also implies that for the best results, two or more successive samples should be taken near the end, since the chances of impurity concentrations being above the detection limit are higher for samples close to the end. In addition, even when only one sample has a detectable impurity concentration, a second closely spaced data point with an upper limit will better constrain k .

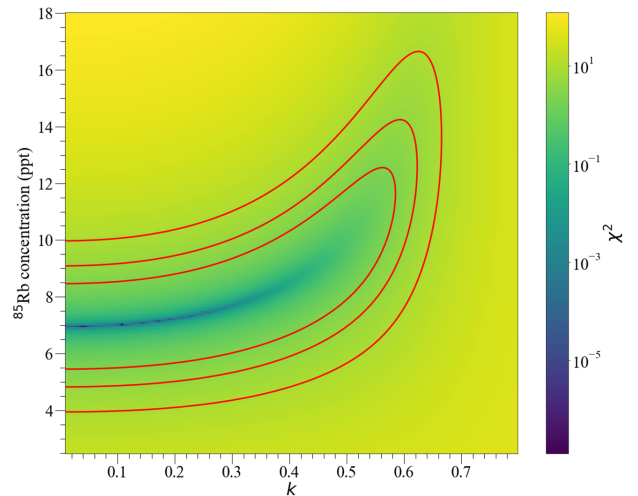


FIG. 8. The χ^2 map for ^{85}Rb is characterized by a band and a series of local minima, since there is only one sample with a concentration above the detection threshold. If there is one more such data point, k will be constrained from below by the inefficiency of the zone refining and the χ^2 map will resemble Fig. 6. The three contour lines correspond to 1- σ , 90% CL, and 99% CL.

V. RESULTS

Fifty-six metal and semimetal elements are analyzed using ICPMS. Although only a few isotopes are relevant in the context of NaI as a low-background scintillator, for completeness the best-fit parameters, estimated confidence intervals or detection limits are summarized in Tables III and IV in the Appendix.

Of the isotopes assayed, K, Rb, and Pb are of particular interest for NaI-based low-background detectors, since these elements have radioactive isotopes that can cause scintillation background events by the emission of low-energy γ rays [11,12]. The measurement results for these isotopes are summarized in Table I and the analysis results are summarized in Table II.

Potassium has a primordial radioisotope, ^{40}K , that can decay by the capture of a K -shell electron to ^{40}Ar with a 10.7% branching ratio. When the accompanying high-energy γ ray escapes the crystal without interaction, the crystal sees 3-keV x rays, or auger electrons, which corresponds to the middle of the region where the dark-matter annual modulation signal is reported [1]. Potassium that naturally occurs on Earth (^{nat}K) mainly consists of 93.258% ^{39}K , 0.012% ^{40}K , and 6.730% ^{41}K . Due to its large natural abundance, ubiquitous presence, and similar chemical properties to Na, ^{40}K is a source of background for ^{nat}K concentrations as low as approximately 10 ppb.

In this study, K is shown to be effectively separated from NaI by zone refining. Figure 5 shows the concentration of ^{39}K as a function of position for the zone-refined ingot. It

TABLE I. The concentrations of impurities of interest at the five sample locations measured using ICPMS. The range after the \pm sign corresponds to the physical size of each sample. The 1σ uncertainties are shown using the parenthesis notation. The upper limits in this table are the 10σ limit of quantification of the spectrometer. A few other isotopes are included to show that zone refining also works for other elements as well.

Isotope	Powder	Impurity concentration (ppb)				
		Sample location (mm)				
		7(7)	325(9)	492(10)	635(20)	783(30)
^{39}K	7.5	< 0.8	< 0.8	1.0(3)	16(1)	460(6)
^{85}Rb	< 0.2	< 0.2	< 0.2	< 0.2	< 0.2	0.7(1)
^{208}Pb	1.0	0.40(3)	0.40(3)	< 0.4	0.50(3)	0.50(3)
^{65}Cu	7	< 2	< 2	< 2	2.0(5)	620(11)
^{133}Cs	44	0.30(1)	0.20(1)	0.50(2)	23.30(5)	760(1)
^{138}Ba	9	0.10(1)	0.20(1)	1.40(4)	19.0(1)	330.0(6)

can be seen that most K is pushed to the end of the ingot. The segregation coefficient is estimated to be 0.57, which is higher than that reported by Gross [7] but is in good agreement with other independent measurements by single crystal growth [9,13]. The agreement with k obtained via crystal growth indicates that at a zone traveling rate of 2 in. h^{-1} , the measured effective segregation coefficient is already very close to the true segregation coefficient. C_0 estimated by the fit is also in excellent agreement with the measurement value of the unprocessed powder.

The primordial radionuclide of rubidium— ^{87}Rb —is a pure β emitter with an endpoint energy of 282 keV. Although it has a long half life (4.8×10^{10} yr), a high natural abundance of 27.8% makes it a potential background for NaI-based dark-matter detectors even at trace levels [9]. ICPMS measurement of Rb is often performed on the stable isotope ^{85}Rb . However, the typical sensitivity to ^{85}Rb is around 0.2 ppb, while ^{87}Rb can still contribute a significant background at this level.

In this work, the sensitivity to ^{85}Rb is further enhanced by the enrichment of ^{85}Rb in the last sample via zone refining. Using the analysis outlined in Sec. IV A, k is constrained to be below 0.58 and C_0 between 5 to 14 parts per trillion (ppt) at the 90% CL (Table III and Fig. 8). This study also indicates that if one needs a better understanding of how Rb redistributes in NaI, then two or more successive samples should be taken near the end where the Rb concentration peaks, since the chances of detecting Rb near the end are higher. With at least two samples with

detectable Rb concentrations, k and C_0 can be precisely determined and the impurity reduction of Rb in future zone refining will be predictable.

The radioisotope of lead— ^{210}Pb —is one of the biggest backgrounds to low-background NaI(Tl) detectors [11–13]. Unlike ^{40}K and ^{87}Rb , ^{210}Pb is produced by the decay of ^{222}Rn and its concentration is not correlated to that of other stable isotopes of lead. Nonetheless, how stable ^{208}Pb redistributes during zone refining can indicate the effectiveness of removing ^{210}Pb . In the five samples studied, the concentrations of ^{208}Pb show a uniform reduction compared to that of the powder but the distribution does not follow the characteristic distribution of zone refining, suggesting that either zone refining is not very effective in removing lead or there is an alternative, more important, transport mechanism for the redistribution of lead. This will be investigated further in a separate study.

VI. DISCUSSIONS

This study shows that zone refining can be used to purify ultrahigh-purity NaI powder to further remove K and Rb impurities very effectively. In addition, the process of zone refining can be employed as a means of enhancing the sensitivity of ICPMS to measure impurities with concentrations normally below the detection limit of the spectrometer.

A. Improving crystal purity

The purification power of zone refining depends on the segregation coefficient k as well as the fraction of the material kept. The smaller k is, the more efficiently impurities move to the end of the ingot, and the more the dirty part of the ingot is discarded, the higher the average purity of the remaining material will be. Figure 9 shows the final relative impurity (K) concentration as a function of the fraction of the ingot reserved after different numbers of zone passes.

TABLE II. The average initial concentrations and segregation coefficients of the isotopes of interest.

Isotope	k	C_0 (ppb)	Powder (ppb)
^{39}K	0.57 ± 0.04	7.6 ± 0.2	7.5
^{85}Rb	< 0.59	(0.005, 0.014)	< 0.2
^{208}Pb	No observable separation		1.0

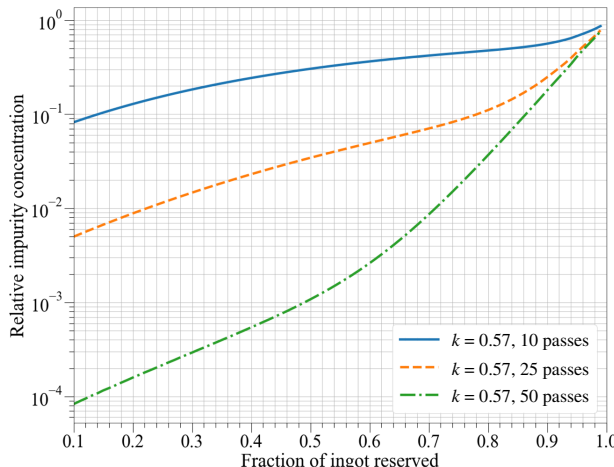


FIG. 9. The impurity reduction as a function of the fraction of material kept after zone refining after 10, 25, and 50 zone passes. The zone width is assumed to be 6% of the length of the ingot and the segregation coefficient is set to be 0.57.

It indicates that after 50 zone passes, the purity of 70% (85%) of the ingot can be improved by a factor of 100 (25). Since the upper limit of k for Rb is also close to 0.57, we expect Rb to be removed at least as efficiently as K during zone refining, and much more efficiently if k is on the order of 0.1 as measured by [7] and estimated from the thermodynamic phase diagram [9,14].

B. Enhancing measurement sensitivity

In the process of zone refining, the impurities are moved toward the ends of the ingot to varying degrees. Due to this enrichment effect, the impurities in the ends can be more easily detected and measured. Given a reasonable model of the system, the original concentration can be constrained using the process outlined in Sec. IV A.

In this study, we constrain the original concentration of ^{85}Rb in the powder to be between 5 and 14 ppt, at least 14 times lower than the detection limit of ICPMS. The initial concentration of ^{87}Rb inferred from ^{85}Rb is 1.9–5.4 ppt. The corresponding activity is $14.4\text{--}40.4 \mu\text{Bq kg}^{-1}$, at least 7 times lower than the most stringent upper limit of $300 \mu\text{Bq kg}^{-1}$ obtained by the DAMA/LIBRA collaboration by direct counting [15].

C. Impact on dark-matter searches

Although recently, the technology to grow large NaI(Tl) crystal with a ^{39}K concentration as low as 4.3 ppb (4.6 ppb ^{nat}K) has been demonstrated [13], most NaI(Tl)-based dark-matter detectors have K concentrations around 30 ppb [11,12]. The projected background due to 30 ppb of ^{nat}K in the absence of active veto is approximately 0.5 counts $\text{day}^{-1} \text{kg}^{-1} \text{keV}^{-1}$ [11,12,16]. If zone refining is used with

70% yield, the background due to ^{40}K can be reduced to 0.005 counts $\text{day}^{-1} \text{kg}^{-1} \text{keV}^{-1}$, which is smaller than 0.01 counts $\text{day}^{-1} \text{kg}^{-1} \text{keV}^{-1}$, the amplitude of the annual modulation.

Unlike K, the concentration of Rb is naturally low in NaI, and no background due to ^{87}Rb has been reported yet. In this study, we constrain the concentration of ^{85}Rb in the ultrahigh-purity NaI powder. The inferred ^{nat}Rb concentration is about 7–19 ppt and the associated ^{87}Rb background is less than 0.02 counts $\text{day}^{-1} \text{kg}^{-1} \text{keV}^{-1}$ in the NaI powder, which is one order of magnitude smaller than other backgrounds due to ^{40}K , ^{210}Pb and ^{3}H [13]. Since all constant nonmodulating backgrounds are suppressed by searching for an annually modulating pattern in the frequency space, a constant background at the same order of magnitude as the modulation amplitude poses little challenge. In addition, crystal growth will reduce the Rb background by at least a factor of 2 based on the upper limit of k and zone refining will further reduce it by at least as much as K is reduced. Thus, in practice, Rb in ultrahigh-purity NaI powder is not a significant source of background.

It must be pointed out that the above estimates are concerned with impurities in the NaI powder. When NaI is doped with Tl to make NaI(Tl) crystal scintillator, the impurities in Tl will typically be diluted by a factor of 1000. If zone refining is used to purify NaI powder of ultrahigh purity, at one point, the final purity will be dominated by the impurities in the Tl dopant instead of NaI.

VII. CONCLUSIONS

Zone refining is performed on ultrahigh-purity NaI powder sealed inside a synthetic fused-silica crucible. By measuring impurity concentrations at different locations of the ingot and comparing them to the numerical model, the segregation coefficients and initial impurity concentrations are calculated for several elements. In addition, using the enrichment effect of zone refining, we also constrain the concentration of Rb in ultrahigh-purity NaI powder, at a level at least 14 times lower than the detection limits of ICPMS and 7 times lower than the previous measurement by direct counting of radioactive ^{87}Rb . During the zone refining, two sources of background, K and Rb, are shown to be efficiently separated from NaI. Calculations indicate that zone refining can easily reduce K and Rb by a factor of between 10 and 100. This indicates that zone refining is an effective and scalable technique to purify ultrahigh-purity NaI powder for next-generation low-background NaI detectors.

ACKNOWLEDGMENTS

We would like to thank Jonathan Mellen and Ashley Mellen at the Mellen Company for help operating

the zone-refining system and Brad McKelvey for help with ICPMS assays. We would also like to thank Aldo Ianni, Masayuki Wada, and Xuefeng Ding for careful reviews of this manuscript and useful discussions, and the two referees of this paper for providing insightful comments and useful suggestions. This research is supported by the National Science Foundation under Awards No. PHY-1242625, No. PHY-1506397, and No. PHY-1620085.

APPENDIX

Fifty-six metal and semimetal elements from different locations of the ingot are analyzed using ICPMS. Of the

TABLE III. A summary of the estimated C_0 and k (best-fit values and $1-\sigma$ errors). When there is only one measurement value, the upper limit of k and the range for C_0 are stated at the 90% CL. Elements marked with an asterisk ("*") show increased concentrations near the dirty end, but the distributions in the clean end deviate noticeably from that expected from zone refining. Elements marked with a dagger ("†") exhibit distributions that are not expected from zone refining. Furthermore, with the exceptions of Ga and Ca, there are noticeable reductions of the total amount of impurities after zone refining, manifesting as either noticeably smaller C_0 compared to the powder or ICPMS values of the zone-refined ingot that are consistently smaller than that of the powder. One explanation is that at such low concentrations, vapor transport is comparable to or more important than zone refining for these elements.

Isotope(s)	k	C_0 (ppb)	Powder (ppb)
^7Li	0.51 ± 0.07	$5.5^{+0.2}_{-0.3}$	2
$^{24}\text{Mg}^*$	0.63	2.7	14
^{39}K	0.57 ± 0.04	7.6 ± 0.2	7.5
^{52}Cr	0.48 ± 0.07	2.1 ± 0.2	< 1
^{56}Fe	0.45 ± 0.07	11.8 ± 1.7	9
^{65}Cu	$0.37^{+0.09}_{-0.12}$	$7.3^{+0.4}_{-0.5}$	7
$^{69}\text{Ga}^*$	0.78 ± 0.02	1.7	1.5
$^{133}\text{Cs}^*$	0.391 ± 0.08	17.1 ± 0.2	44
$^{138}\text{Ba}^*$	0.61 ± 0.04	6.2 ± 0.1	9
^{55}Mn	< 0.37	(0.29, 0.37)	< 0.5
^{59}Co	< 0.95	(0.01, 0.42)	< 0.5
^{60}Ni	< 0.58	(0.39, 1.10)	< 10
^{68}Zn	< 0.70	(0.08, 0.44)	< 13
^{85}Rb	< 0.59	(0.005, 0.014)	< 0.2
^{88}Sr	> 1.4	(0.08, 0.44)	< 0.1
^{89}Y	< 0.50	(0.0, 0.05)	< 0.1
^{90}Zr	< 0.76	(0.01, 0.10)	< 2
^{139}La	< 0.31	(0.15, 0.2)	< 1
^{172}Yb	> 1	(0.0, 0.09)	< 0.1
$^{27}\text{Al}^{\dagger}$			3
$^{44}\text{Ca}^{\dagger}$	Irregular distribution		130
$^{48}\text{Ti}^{\dagger}$			2
$^{208}\text{Pb}^{\dagger}$			1

TABLE IV. A summary of isotopes the concentrations of which are below the detection limit in all the samples.

Isotope	C_0 (ppb)
^{238}U	< 0.1
^{153}Eu , ^{165}Ho , ^{175}Lu , ^{197}Au	< 0.2
^{51}V , ^{149}Sm , ^{169}Tm	< 0.5
^{178}Hf , ^{187}Re	< 0.8
^{232}Th	< 0.8
^9Be , ^{93}Nb , ^{111}Cd , ^{146}Nd	< 1
^{157}Gd , ^{181}Ta , ^{195}Pt	< 5
^{98}Mo , ^{107}Ag	< 10
^{11}B , ^{72}Ge , ^{75}As , ^{105}Pd	< 10
^{121}Sb , ^{141}Pr , ^{166}Er	< 20
^{209}Bi	< 50
^{102}Ru , ^{182}W	< 100
^{45}Sc , ^{103}Rh	

elements analyzed, zone refining is confirmed to be effective for about 20 elements. These elements are listed in Table III. Due to the already very high purity of the starting raw powder, only about half of these 20 elements have detectable concentrations in more than two samples. Table IV lists elements whose concentrations are too low, compared to the detection limit of the spectrometer, to be detected in any of the five samples.

- [1] R. Bernabei, P. Belli, A. Bussolotti, F. Cappella, V. Caracciolo, R. Cerulli, C.-J. Dai, A. d'Angelo, A. Di Marco, and H.-L. He *et al.*, First model independent results from DAMA/LIBRA—phase2, *Universe* **4**, 116 (2018).
- [2] J. Amaré, S. Cebrián, I. Coarasa, C. Cuesta, E. García, M. Martínez, M. Oliván, Y. Ortigoza, A. O. de Solórzano, and J. Puimedón *et al.*, First Results on Dark Matter Annual Modulation from the ANAIS-112 Experiment, *Phys. Rev. Lett.* **123**, 031301 (2019).
- [3] G. Adhikari, P. Adhikari, E. B. de Souza, N. Carlin, S. Choi, M. Djamal, A. Ezeribe, C. Ha, I. Hahn, and E. Jeon *et al.*, Search for a Dark Matter-Induced Annual Modulation Signal in NaI(Tl) with the COSINE-100 Experiment, *Phys. Rev. Lett.* **123**, 031302 (2019).
- [4] M. Antonello, E. Barberio, T. Baroncelli, J. Benziger, L. Bignell, I. Bolognino, F. Calaprice, S. Copello, D. D'angelo, and G. D'imperio *et al.*, The SABRE project and the SABRE proof-of-principle, *Eur. Phys. J. C* **79**, 1 (2019).
- [5] G. Angloher, P. Carniti, L. Cassina, L. Gironi, C. Gotti, A. Gütlein, M. Maino, M. Mancuso, L. Pagnanini, and G. Pessina *et al.*, Results from the first cryogenic NaI detector for the COSINUS project, *J. Instrum.* **12**, P11007 (2017).
- [6] W. G. Pfann, Principles of zone-melting, *JOM* **4**, 747 (1952).
- [7] U. Gross, Zone purification of alkali iodides, *Mater. Res. Bull.* **5**, 117 (1970).
- [8] J. Verhoogen, Ionic diffusion and electrical conductivity in quartz, *Am. Mineral.*: *J. Earth Planet. Mater.* **37**, 637 (1952).

- [9] Suerfu, Ph.D. thesis, Princeton University (2018).
- [10] J. Eckstein, U. Gross, and E. Rubinová, Growth of alkali halide crystals with a lowered concentration of oxygenous anions using SiX₄ as a removing agent, *Kristall und Technik* **3**, 583 (1968).
- [11] J. Amaré, S. Cebrián, I. Coarasa, C. Cuesta, E. García, M. Martínez, M. Oliván, Y. Ortigoza, A. O. de Solórzano, and J. Puimedón *et al.*, Analysis of backgrounds for the ANAIS-112 dark matter experiment, *Eur. Phys. J. C* **79**, 412 (2019).
- [12] P. Adhikari, G. Adhikari, E. B. de Souza, N. Carlin, S. Choi, W. Choi, M. Djamal, A. Ezeribe, C. Ha, and I. Hahn *et al.*, Background model for the NaI(Tl) crystals in COSINE-100, *Eur. Phys. J. C* **78**, 490 (2018).
- [13] B. Suerfu, M. Wada, W. Peloso, M. Souza, F. Calaprice, J. Tower, and G. Ciampi, Growth of ultra-high purity NaI(Tl) crystals for dark matter searches, *Phys. Rev. Res.* **2**, 013223 (2020).
- [14] C. Bale, E. Bélisle, P. Chartrand, S. Dechterov, G. Eriks-son, K. Hack, I.-H. Jung, Y.-B. Kang, J. Melançon, and A. Pelton *et al.*, FactSage thermochemical software and databases—recent developments, *Calphad* **33**, 295 (2009).
- [15] R. Bernabei, P. Belli, A. Bussolotti, F. Cappella, R. Cerulli, C. Dai, A. d'Angelo, H. He, A. Incicchitti, and H. Kuang *et al.*, The DAMA/LIBRA apparatus, *Nucl. Instrum. Methods Phys. Res. Sec. A: Accelerators, Spectrometers, Detectors Associated Equipment* **592**, 297 (2008).
- [16] M. Antonello, E. Barberio, T. Baroncelli, J. Benziger, L. Bignell, I. Bolognino, and F. Calaprice *et al.*, Monte Carlo simulation of the SABRE PoP background, *Astropart. Phys.* **106**, 1 (2019).